Late Holocene peat paleodust deposition in south-western Sweden - exploring geochemical properties, local mineral sources and regional aeolian activity

J.K. Sjöström, R. Bindler, A. Martínez Cortizas, S. Björck, Sophia V. Hansson, A. Karlsson, D.T. Ellerton, M.E. Kylander

Chemical Geology 602 (2022) 120881

Contents lists available at ScienceDirect

Chemical Geology

journal homepage: www.elsevier.com/locate/chemgeo

Late Holocene peat paleodust deposition in south-western Sweden - exploring geochemical properties, local mineral sources and regional aeolian activity

J.K. Sjöström [a,b,*], R. Bindler [c], A. Martínez Cortizas [d], S. Björck [e], S.V. Hansson [f], A. Karlsson [g], D.T. Ellerton [a,b], M.E. Kylander [a,b]

[a] Department of Geological Sciences, Stockholm University, Stockholm, Sweden
[b] Bolin Centre for Climate Research, Stockholm, Sweden
[c] Department of Ecology and Environmental Science, Umeå University, Umeå, Sweden
[d] CRETUS, EcoPast (GI-1553), Universidad de Santiago de Compostela, Santiago de Compostela, Spain
[e] Department of Geology, Lund University, Lund, Sweden
[f] Laboratoire écologie fonctionnelle et environnement, CNRS Université de Toulouse, Toulouse, France
[g] Department of Geosciences, Swedish Museum of Natural History, Stockholm, Sweden

ARTICLE INFO

Editor: Dr. Karen Johannesson

Keywords:
Peat
Mineral dust
Peat accumulation rate
Storms
Carbon accumulation
Fertilization

ABSTRACT

Atmospheric mineral dust not only interacts with the climate system by scattering incoming solar radiation and affecting atmospheric photochemistry, but also contributes critical nutrients to marine and terrestrial ecosystems. In a high-resolution analysis of paleodust deposition, peat development and soil dust sources, we assess the interplay between dust deposition and bog development of the Davidsmosse bog in south-western Sweden. Analyses of the 5400-year record (458 cm) included radiocarbon dating, bulk density, ash content, chemical and mineralogical composition and carbon stable isotopes, subsequently explored using principal component analysis. Fourteen dust events (DEs) were recorded (cal BP) in the peat sequence: 3580–3490; 3280; 3140; 3010–2840; 2740; 2610; 2480; 2340; 2240–2130; 1690; 1240; 960, 890–760, and 620–360. The majority of the DEs were coupled to increases in peat accumulation rates and increased nutrient content (N, P and K) suggesting that the DEs contributed with nutrients to the bog ecosystem, promoting increased accumulation. We also analyzed the chemical and mineral composition of potential mineral source deposits (separated into 6 grain-size fractions) from sites within a 4 km radius as well as aeolian dunes closer to the coast (25 km). The composition deposited on the present-day bog surface indicates that the bulk of the contemporary minerals have a local origin (<1.5 km), but the DEs may be of a more distant origin. The results also indicate that quartz and plagioclase feldspar content consistently increase with increasing grain-size, both in the source samples as well as in the peat sequence, and that the Si/Al ratio can be used to infer grain size changes in the peat. Two longer phases saw numerous DEs, between 2800 and 2130 cal BP and a stepwise increase from 960 towards 360 cal BP. The episodic character of the events, together with the inferred coarse grain size, suggest that the particles were deposited by (winter) storms. Future studies should include grain size analysis as well as a more in-depth comparison with regional paleo dust and storm records to increase knowledge on both transport processes (creep, saltation, suspension) and the climate processes driving late Holocene dust and storm events in Scandinavia.

Abbreviations: calendar years before present, Cal BP; dust event, DE; principal component analysis, PCA; powder X-ray diffraction, pXRD; scanning electron microscope – energy dispersive spectroscopy, SEM-EDS; wave-length dispersive X-ray fluorescence, WD-XRF; accelerator mass spectrometry, AMS; north atlantic oscillation, NAO.

* Corresponding author at: Stockholm University, Dept. of Geological Sciences, S-106 91 Stockholm, Sweden.
E-mail address: jenny.sjostrom@geo.su.se (J.K. Sjöström).

https://doi.org/10.1016/j.chemgeo.2022.120881
Received 26 November 2021; Received in revised form 22 March 2022; Accepted 20 April 2022
Available online 26 April 2022

1. Introduction

Atmospheric mineral dust interacts with Earth's climate system by affecting incoming solar radiation, atmospheric chemistry, cloud formation, and by contributing with essential nutrients to marine and terrestrial ecosystems (Knippertz and Stuut, 2014; Yu et al., 2015; Albani et al., 2015; Kylander et al., 2018; Gu et al., 2019). To date, Holocene paleodust reconstructions have focused mainly on lower-latitude marine sediment cores or higher-latitude polar ice cores, with less attention paid to terrestrial records from the mid-latitudes (Harrison et al., 2001). While marine records capture dust loads from distant sources, continental records (e.g., lakes, loess, and bogs) also receive inputs of mineral particles derived from local and regional sources. Regional terrestrial dust loads are affected not only by climate factors, but also by a range of human activities such as forestry, agriculture, and industrial activities (Martínez Cortizas et al., 2005; Kylander et al., 2005; De Vleeschouwer et al., 2012; Silva-Sánchez et al., 2014).

Reconstructions of paleodust deposition in peat sequences are achieved through down-core geochemical analysis of conservative lithophile elements such as Sc, Ti, Zr, or rare earth elements (REE) (Steinmann and Shotyk, 1997; Shotyk et al., 2002; Aubert et al., 2006) which are used to infer changes in dust deposition rates, mineralogy, grain size and provenance. To date, a number of geochemical approaches have been applied to study changes in the grain size, mineralogy and, thereby, source of dust deposited in peatlands, e.g., Pb and Nd isotope analyses (Kylander et al., 2005; De Vleeschouwer et al., 2012; Li et al., 2020), particle-size analysis (Panait et al., 2019; Pratte et al., 2019) and/or elemental ratios (Shotyk et al., 2002; Kylander et al., 2016). Elemental ratios can be used to infer changes in grain size or mineralogy because some elements are enriched or depleted in certain grain sizes and/or mineral groups.

Current challenges within paleodust studies of ombrotrophic (rain-fed) bogs include identifying peatland succession and the relative importance of fluvial and aeolian transport processes (Sjöström et al., 2020), identifying and separating local from regional sources within dust events (Shotyk et al., 2001; Albani et al., 2015), separating detrital from authigenic minerals (López-Buendía et al., 2007; Rudmin et al., 2018; Sjöström et al., 2020) and establishing a reliable proxy for quantifying dust deposition (Shotyk et al., 2002; Kylander et al., 2016; Martínez Cortizas et al., 2019).

Few peat paleodust studies have included an assessment of local dust sources, limiting the understanding of how mineral composition (i.e., grain size, mineralogy, geochemistry) may vary with, as well as within, different local sources. Here, we sampled and analyzed a peat sequence from Davidsmosse, ~30 km from the coast, south-western Sweden. The specific objectives were to: 1) reconstruct peat accumulation rates, paleodust deposition and mineral composition in the Davidsmosse peat sequence; 2) determine the mineralogical and geochemical fingerprint of local sources; and 3) explore the links between local sources, dust events and peat accumulation rates through time. To address these objectives, we analyzed a 458-cm-long peat sequence from Davidsmosse for its botanical composition, bulk density, peat accumulation rate, ash content, major and trace elemental geochemistry (WD-XRF), mineral composition (pXRD), and radiocarbon dating of peat plant macrofossils. The resolution of the analyses varied by analytical approach. To obtain information on the mineral composition deposited currently at Davidsmosse, a living vegetation sample (20 × 30 cm) from the bog surface was also collected from the coring location, subsequently analysed by pXRD. In addition to the peat sequence, we sampled potential dust sources, which included five sites located within a 4 km radius of Davidsmosse representing the dominant soil and sediments in the area, and two aeolian dune samples located at the coast, 35 km west of our study site. These samples were separated into 6 grain-size fractions that were analyzed for chemical and mineralogical composition.

1.1. Study site

Davidsmosse (56° 59′ 10" N, 13° 00' 32" E, 170 ha, m a.s.l. 143 m) is located 30 km from the west coast in the eastern part of the Halland province, south-western Sweden (Fig. 1). The bog is located in the Nissan catchment area, which drains towards the south-west to the Kattegat Sea. The study site is located in a maritime climate, with a contemporary average annual temperature of 7 °C, 1050–1125 mm annual precipitation, 7.3 m s^{-1} average wind strength, and westerly winds dominate (Alexandersson, 2006; SMHI, 2009). The growing season in the area (i.e., starting from the first 4 days above 5 °C) is 230–240 days (SMHI, 2015).

Geologically the area consists of granitic gneisses of 1.74–1.66 Ga age, with local occurrences of syenite and amphibolites (Samuelsson and Larson, 1987). The Halland region was deglaciated between 16 and 15 Ka (Lundqvist and Wohlfarth, 2001; Stroeven et al., 2016) and was above the marine limit both during and following deglaciation (Påsse, 1993). The current bog vegetation is dominated by *Sphagnum* mosses together with heather and sedges, while the mire edges are forested by pine trees. Davidsmosse has two distinct lobes, separated by a forested area, with our study site located in the larger, eastern lobe. Local soils are dominated by till, glaciofluvial sediments and peat (Påsse, 1993. Fig. 1).

2. Materials and methods

2.1. Core retrieval, subsampling, bulk density and loss on ignition (LOI)

The peat sequence was collected in May 2014 with a Russian peat corer (100 × 7.5 cm barrel), reaching a total depth of 488 cm. Seven one-meter cores with 25-cm overlap were retrieved from two alternating boreholes. The uppermost 30 cm was not collected. The cores were stored frozen (−18 °C), cut into 1-cm slices with a stainless-steel band saw, followed by freeze-drying. The volume and dry weight of each slice were measured to calculate bulk density ($n = 458$) (Givelet et al., 2004), which was used to align the cores and make a composite sequence of 458 cm. Loss-on-ignition (LOI), the weight loss after combustion at 550 °C (Dean, 1974), was determined at 1 to 3 cm intervals ($n = 193$).

2.2. Local source samples

Seven local source samples were collected (~500 g, 30–50 cm below the surface) in August 2020 (Fig. 1). The samples were insonicated and wet sieved into six size fractions (>500; 500–250; 250–150; 150–63; 63–38; and < 38 μm) using standard sieves. The respective residues were dried (105 °C) and weighed to calculate the relative grain size distributions, followed by analysis for both mineralogical (pXRD) and chemical content (WD-XRF), described further below.

2.3. Radiocarbon dating and chronology

Six macrofossil samples were sent for AMS radiocarbon dating to Beta Analytic Inc. ($n = 5$; Miami, FL, USA) and the Radiocarbon Laboratory (n = 1; Uppsala University, Sweden) (Table 1). Peat samples were wet sieved in deionized water, the >125 μm residues put in a petri dish and suitable macro-fossils were picked out under a light microscope (10-40× magnification), guided by Wohlfarth et al. (1998), Mauquoy and van Geel (2007) and Mauquoy et al. (2010). Calibration and age–depth modelling (Fig. 2) were conducted using Bacon (Blaauw and Christen, 2011), version 2.5, which includes the IntCal20 ^{14}C calibration curve (Reimer et al., 2020). The acquired weighted mean and the accumulation rate (cm yr^{-1}), together with the bulk density, were used to calculate peat accumulation rate, ash accumulation rate and elemental mass accumulation rates (PAR, AAR and MAR, respectively), as well as to plot data on a calendar age scale.

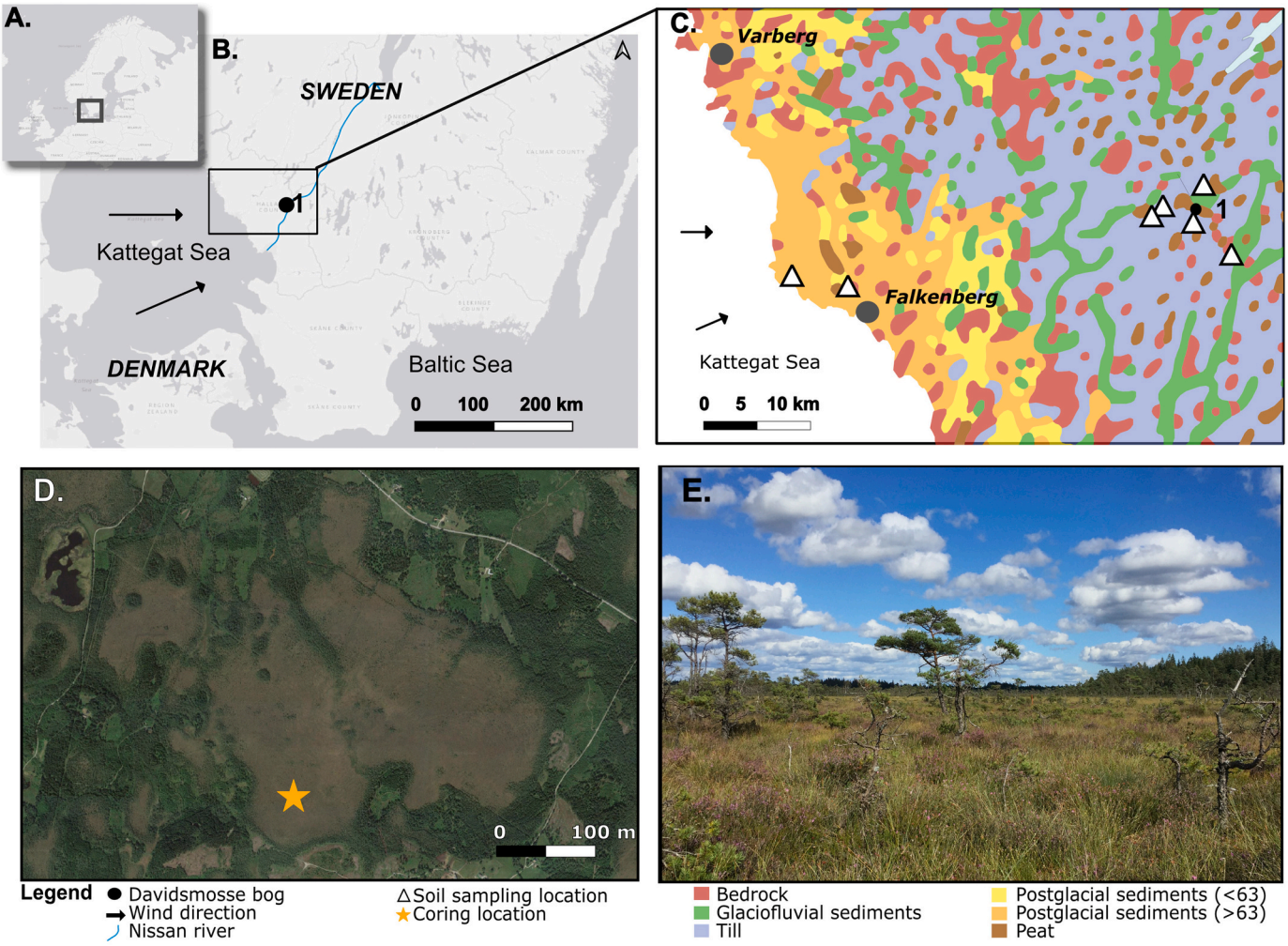

Fig. 1. (A.) Orientation map, (B.) regional map, including the location of the current study site (black dot), (C.) quaternary deposits map, including sample locations (triangles) and Davidsmosse bog (black dot), (D.) satellite image of Davidsmosse, (E.) picture from coring location. Maps based on SGU open database (www.sgu.se), ESRI Grey and Google satellite (2020), compiled and edited in QGIS, ver. 3.10.

Table 1
Result of radiocarbon dating. Calibration and age-depth model constructed using Bacon (Blaauw and Christen, 2011), version 2.5.

Depth (cm)	Laboratory ID	Material Used for Dating	^{14}C yr ±1σ	Calibrated Age Range, BP. 2σ
120	Beta414244	Sphagnum leaves and stems	1720 ± 30	1710–1555
193	Beta414240	Sphagnum leaves and stems	2430 ± 30	2700–2355
304	Beta414241	Sphagnum leaves and stems	3220 ± 30	3545–3380
411	Beta414242	Sphagnum leaves and stems	3950 ± 30	4515–4300
468	Ua52055	Sphagnum leaves, betula and larix seeds.	4419 ± 30	5290–4860
487	Beta414243	Insect and plant remains	4630 ± 30	5455–5305

2.4. Elemental analysis

Total C and N as well as stable isotopes of carbon (δ^{13}C) of the bulk peat samples were measured using a Carlo Erba NC2500 elemental analyzer, coupled to a Finnigan MAT Delta + mass spectrometer at the Department of Geological Sciences, Stockholm University. The relative error for the measurement was <3%. The δ^{13}C data are reported in per mil (‰) relative to V-PDB. WD-XRF analysis on both peat and soil samples was conducted at the Department of Ecology and Environmental Science, Umeå University, in a Bruker X8-Tiger analyzer equipped with a Rh-anticathode X-ray tube. Peat elemental concentrations were measured in dried and milled subsamples (400–500 mg), which were placed in plastic cups covered with 2.5 μm Mylar® film, using a calibration method developed by Rydberg (2014), adapted to peat and plant samples by Hansson et al. (2013). The analytical performance was assessed through SRM NIST-8437 (Hard Red Spring Wheat Flour) and by replicate analysis of a previously measured internal peat sample. Accuracy was calculated as the relative difference between the average concentration and the certified values of the SRM. Precision was calculated as the relative standard deviation of repeated measurements of the SRM and of peat samples. Precision ($n = 9$ NIST-8437, $n = 6$ peat) was within ±10% (or a few ppm) for Al, Ca, Cl, P, K, Mg Ca, S, Si, Ti, Fe, and Sr with slightly higher values noted for Na (±13%). Accuracy for P, K, Ca, Fe and Zn was within ±10%, while remaining elements were below the detection limit in the SRM. Replicate analysis of the internal peat standard indicated accuracy was within ±10%. The surface source

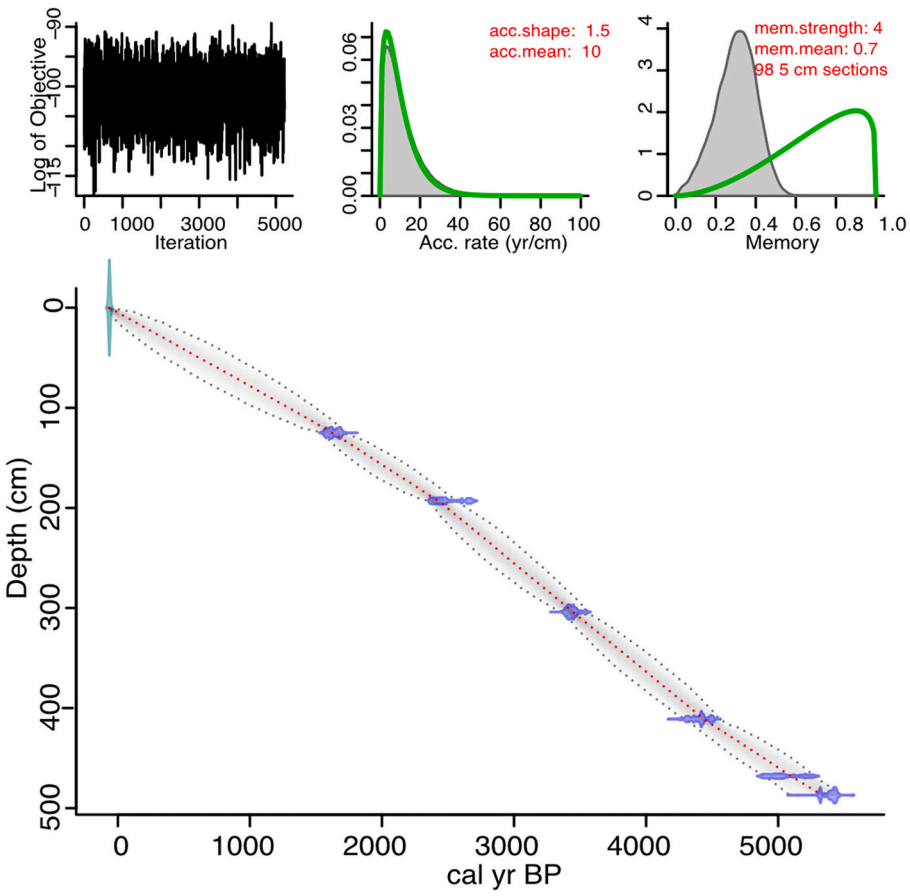

Fig. 2. Age-depth model for Davidsmosse. Calibrated probability distributions of the six ^{14}C dates are shown in blue. The red dotted line represents the weighted mean of the age-depth model, and the grey shading indicates the 95% confidence range. The three top boxes show information about the model, from the left: quality of the iteration; predicted (grey shape) versus actual mean (green line), and values used in the a priori information used in the Bayesian approach (Blaauw and Christen, 2011). (For interpretation of the references to color in this figure legend, the reader is referred to the web version of this article.)

samples were analyzed using 200 mg of finely milled sample using the calibration developed by Rydberg (2014), with reported accuracies within ±10% and precision within ±5% (except for Br, 18%).

2.5. Statistical analysis

Principal component analysis (PCA) was applied to explore statistical associations of the peat sequence and source samples. The PCA for the peat samples was based on the elemental data, AAR and bulk density, while the PCA on the surface samples only included elemental data. Analysis was done in JMP 15, applying a correlation mode with a varimax rotation. For the peat sequence ($n = 126$), concentration values from the WD-XRF analysis were calculated to MAR (concentration x peat accumulation rate), screened for outliers, and subsequently converted to z-scores following (Martínez Cortizas et al., 2019). The source samples data-set was also converted to z-scores. By transforming values to z-scores the data are transformed to average-centered distributions (Eriksson et al., 1999), which avoids scaling effects. The z-scores were calculated as:

$$Z = (X - \mu)/\sigma \quad (1)$$

where Z represents the z-score, X is the measured value at each data point (depth), μ represents the average value of each variable and σ represents one sigma standard deviation of the variable.

2.6. Powder X-ray diffraction (pXRD) analysis

The pre-treatment of ashed peat samples followed Sjöström et al. (2019). The source samples were analyzed following the pre-treatment described in section 2.2. The sample from the current bog surface, was soaked in deionized water and insonicated to wash out detrital minerals. The water was thereafter evaporated and the residue ignited at 500 °C to remove organic matter (Sjöström et al., 2019). All samples were milled into a fine powder prior to analysis. pXRD analyses were conducted at the Swedish Museum of Natural History, Stockholm, using a PANalytical X–ray diffraction system (X'Pert^3 Powder) equipped with a multi detector. The samples were analyzed from 5° to 70° 2θ, with CuKα radiation (λ = 1.5406 Å) at 45 kV and 40 mA, passing through a curved graphite monochromator, fixed divergence and receiving slits (1°), step size 0.017° and a count time of 38 s. Processing of the diffractograms, such as determination of background, smoothing, peak localization, mineral identification and quantification, was done in HighScore 4.6, a PANalytical software (Degen et al., 2014) with integrated mineral reference patterns from the ICSD database (2012). Brindley and Brown (1984) and Moore and Reynolds (1997) were also used to guide mineral identification. The Rietveld refinement method (Rietveld, 1969), which quantifies the relative occurrence of the mineral phases, was conducted (5–55° 2θ) using the HighScore default settings (Degen et al., 2014).

2.7. Scanning Electron Microscope – Energy Dispersive Spectroscopy (SEM-EDS) analysis

To verify the pXRD mineral identification and chemical composition, two samples were also analyzed by SEM-EDS. One source sample (3A > 500 μm) and one ashed peat sample (C3, 34–45) were mounted in epoxy resin, polished with 3 μm and 1 μm diamond spray (Akasel) to expose a cross-section of the mineral grains, and coated with carbon. A FEI Quanta 650 field emission scanning electron microscope, fitted with an 80 mm^2 X-Max^N Oxford Instruments EDS detector (working distance 10 mm, beam size >1 μm, acceleration voltage 20 kV), was used to determine the composition. The instrument was calibrated against metal and mineral standards for each individual element, while the beam current

was calibrated on Co metal.

3. Results

3.1. Radiocarbon ages and age-depth model

The lowermost sample showed a calibrated age of 5335 cal BP (weighted mean), indicating that the sequence has been accumulating the last 5400 years (Table 1). The results of the age-depth modelling show that the average temporal resolution of Davidsmosse is 11 ± 3.5 yr cm^{-1} (average ± 2σ standard deviation, Fig. 2). All results reported in the following sections are described relative to the calendar ages (mean cal BP) rounded to the nearest decade.

3.2. Peat properties

Between c. 5350 and 5230 cal BP the peat mainly consists of Carex and woody fragments. After 5230 cal BP the woody fragments disappear and *Carex* dominates the peat until 4760 cal BP when *Sphagnum* mosses appear (Fig. 3). *Sphagnum* mosses dominate from 4610 cal BP towards the present, with sedges reappearing at (cal BP): 4270–4130; 3820–3620; 3440; 2960–2830; 2160; and 2090–1400 (Fig. 3). The uppermost part of the sequence, 440–340 cal BP, is dominated by roots from the surface vegetation. The bulk density varies from 0.04 to 0.18 g cm^{-3} (average: 0.08 ± 0.05 g cm^{-3}, n = 458, all standard deviations here are given as 2σ) throughout the sequence, with higher values occurring in the oldest (5350–4600 cal BP, 0.12 ± 0.06 g cm^{-3}, n = 73) and most recent (0.12 ± 0.05 g cm^{-3}, n = 20) sections of the record (Fig. 3). The peat accumulation rate ranges from 29 to 202 g m^{-2} yr^{-1} (average: 73 ± 42 g m^{-2} yr^{-1}, n = 462). Because of the nearly linear age-depth model (Fig. 2), the peat accumulation rate profile follows the trend of bulk density, with higher values noted in the lowermost, *Carex* part, of the sequence (5350–4670 cal BP) and in the *Sphagnum*-dominated section (cal BP): 4610–4530; 4280–4000; 3940–3770; 3640–3455; 3020–2880; 2230; 2180–2150; 1860; 1920; 1005–920; 900–830; and 610–340. The ash content varies from 0.8 to 6.4% (average: 1.3 ± 1.6%, n = 191) with the highest concentration noted at 410 cal BP. The AAR varies from 0.2 to 6.3 g m^{-2} yr^{-1} (average value 1.1 ± 1.9 g m^{-2} yr^{-1}, n = 191), with the highest values occurring from 450 to 360 cal BP (5.8 ± 1.4, g m^{-2} yr^{-1}, n = 4).

Carbon accumulation rates (CAR) range from 16 to 117 g m^{-2} yr^{-1} (average 41 ± 32 g m^{-2} yr^{-1}, n = 96), while N accumulation range from 0.2 to 3.5 g m^{-2} yr^{-1} (average 0.9 ± 1.2 g m^{-2} yr^{-1}, n = 96). The two profiles largely follow each other, but with larger variability recorded in the N as compared to C accumulation rates. The C/N profile average is 66 ± 17 (n = 96) with above average values noted at (cal BP): 4450 (n = 2); 4075 (n = 2); 3910–3670 (n = 7); 2700–2650 (n = 2); 2570–2510 (n = 2); 2450–2390 (n = 2); 2270 (n = 1); 1980–1920 (n = 2); 1810–1750 (n = 2); and 1630–1300 (n = 6). Lower C/N values were recorded between (cal BP) 5350–4530 (n = 16) and 4370–4140 (n = 6). In-between these trends, episodic drops are also observed (Fig. 3), particularly after 3000 cal BP. From 1130 cal BP towards the top the C/N values decrease. δ^{13}C values range from −28.5 to −25.1‰ (average 26.7 ± 1.4‰, n = 81) and largely follow the C/N profile but with a lower magnitude of the variability.

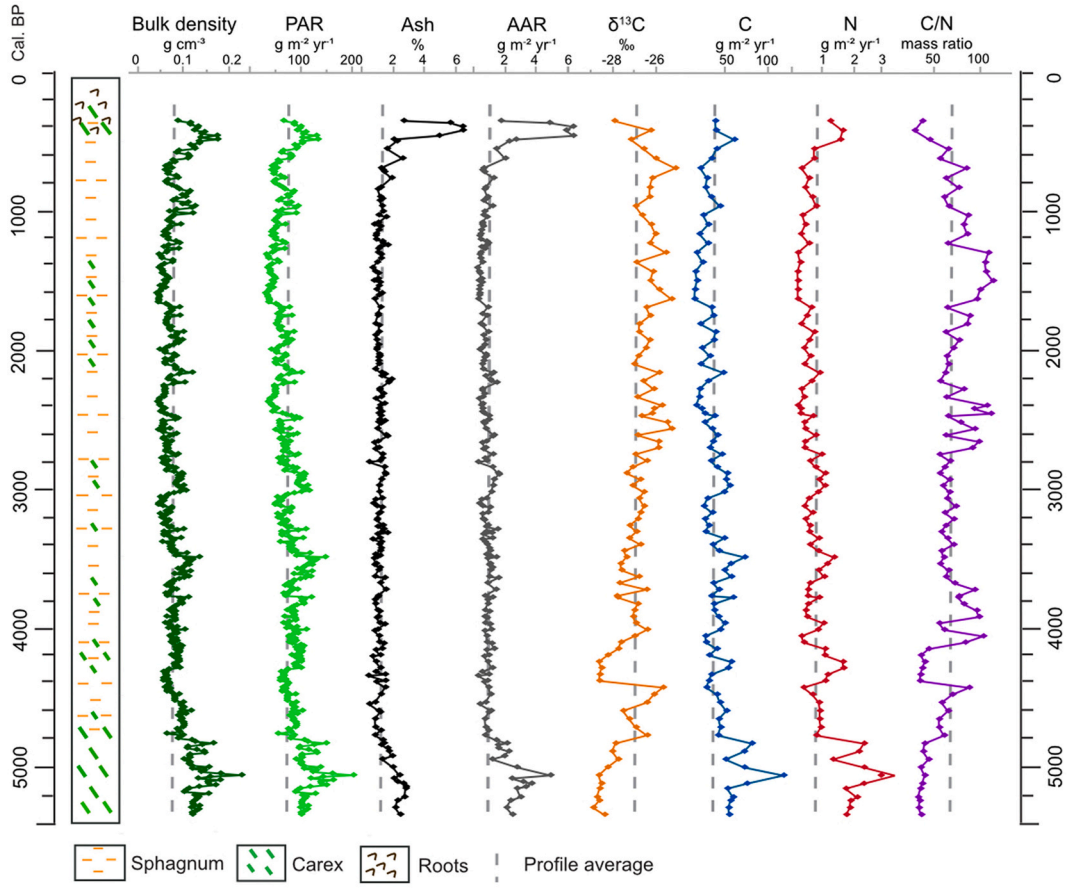

Fig. 3. Peat composition, bulk density, peat accumulation rate (PAR), ash content, ash accumulation rate (AAR), δ^{13}C, carbon accumulation rate, nitrogen accumulation rate, and C/N and plotted against age. The profile average for each parameter is indicated by a dotted grey line. For a version depicting these results plotted against depth, please see the Appendix (A.Fig. 1). (For interpretation of the references to color in this figure legend, the reader is referred to the web version of this article.)

3.3. WD-XRF, principal component analysis and elemental ratios

3.3.1. Peat sequence

Based on the analytical performance and relevance to the study objectives a number of elemental MARs were selected from the WD-XRF analysis of the peat sequence (Al, Br, Ca, Cl, Fe, K, Na, Mg, S, Si, Ti, P, and Sr). The individual MAR profiles can be viewed in the appendix (A. Fig. 2). Two samples from the uppermost part of the sequence were not included in the PCA because they displayed highly elevated values and therefore had a disproportionate effect on the z-scores and the extraction of components in the PCA (Eriksson et al., 1999). In the PCA, three components (CP) account for at least 85% of the total variance (Table 2). The first component (CP1) accounts for 39% of the variance and very strongly associated (>0.9) variables include Fe and Ca, while AAR, S, bulk density and P are strongly associated (0.7–0.9) (Table 2). CP2 accounts for 28% of the total variance with Si, Ti, and Al very strongly associated, while Br is strongly associated. Chlorine, K, Sr, S, AAR and bulk density are moderately associated (0.3–0.7). CP3 accounts for 19% of the total variance with Mg and Cl strongly associated, while Na, K, Sr and Br are moderately associated. A few variables are almost equally associated to two or more components: Br, Cl, K, Na and Sr.

Plotting the factor scores against age provides a visual representation of the variability of the components with time (Fig. 4) (e.g. Martínez Cortizas et al., 2019). The profiles show deviations from the average (0). CP1 is highly elevated between 5350 and 4830 cal BP, followed by slightly positive values until 4150 cal BP. After this, below-average values are recorded towards the present. CP2 displays a general, but stepwise, decrease from 5340 cal BP, followed by below-average values between 4940 and 3630 cal BP (n = 28). Thereafter, fourteen (1–14) above-average (>0.1) episodes are noted at (cal BP): 1) 3580–3490 (n = 3); 2) 3280 (n = 1); 3) 3140 (n = 2); 4) 3010–2840 (n = 5); 5) 2740 (n = 1); 6) 2610; 7) 2480 (n = 2); 8) 2340 (n = 1); 9) 2240–2130 (n = 8); 10) 1690 (n = 1); 11) 1220 (n = 2); 12) 960 (n = 1), 13) 890–760 (n = 2) and 14) 615–490. Minor increases (>0.01) are noted at (cal BP): 2050, 1890 and 1360. CP3 is generally below average between 5350 and 4420 cal BP (n = 19), except for an above-average peak centered around 5030 cal BP (n = 2). Between 4380 and 2610 cal BP above-average scores are noted, followed by variable, but mostly below-average values. The two uppermost samples show above-average values.

To explore changes in mineral composition and grain size, two elemental ratios were plotted for the peat sequence: Si/Ti and Si/Al (Fig. 4). The Si/Ti ratio ranges from 10 to 50 (average: 27 ± 15) with the lowest values recorded in the lowermost part of the sequence, while the highest occur in the uppermost parts of the sequence. Between 5350 and 4990 cal BP the ratio stays below the average, followed by an increase until 3870 cal BP. The ratio thereafter decreases until 3125 cal BP. Around average values are again noted between 3070 and 2660 cal BP, followed by greater variability until 1920 cal BP. The value thereafter stays around the average until 1530 cal BP, after which a decrease occurs. Below-average values are then noted until 1270 cal BP. The value thereafter generally increases, with peaks noted at (cal BP): 1040; 840; 615; and 360.

The Si/Al ratio averages around 1.6 ± 1.4 with below average values noted in the lowermost part of the sequence (5350–5050 cal BP). Between 5000 and 2920 cal BP around average, and a decreasing trend, is recorded. From 2880 cal BP and onwards greater variability, and overall higher values, are recorded, with peaks noted at (cal BP): 2880; 2610; 2490; 2340; 2200; 2050; 1690; 1400; 1240; 960; 760; 615; and 410. Highly elevated values and an increasing trend is noted from 1040 until 410 cal BP.

Table 2
Result of the PCA analysis of the WD-XRF peat samples.

Variables	CP1	CP2	CP3
Expl. var. %	39%	28%	19%
Cum. var. %	39%	67%	86%
Fe	**0.99**	0.00	−0.15
Ca	**0.94**	0.12	0.28
AAR	**0.90**	0.34	0.10
S	**0.89**	0.33	0.19
Bd	**0.78**	0.33	0.25
P	**0.77**	0.13	0.07
Sr	0.66	0.45	0.55
Si	0.06	**0.95**	0.05
Al	0.29	**0.91**	0.21
Ti	0.37	**0.91**	0.08
Br	0.23	**0.71**	0.47
Mg	−0.07	−0.02	**0.86**
Cl	0.09	0.54	**0.74**
Na	0.47	0.17	0.64
K	0.51	0.49	0.61

3.3.2. Surface source samples

The chemical composition of the surface source samples, including grain size distributions, is found in Appendix A (A.Table 1) (n = 42). The results show that grains over 63 μm dominate over smaller grain sizes in all samples, and that sizes >500 μm dominate in four samples (3A, 8B, 6B, 7A) (A.Table 1). The two dune samples (9AB and 11B) are well sorted, dominated by two size fractions: 150–250 μm (41% and 53%, respectively) and 250–500 μm (48% and 35%, respectively). In total 40 sub-samples (A.Table 1) were analyzed by WD-XRF (two subsamples, 11B: <38 and 38–63 μm, had insufficient sample weight for XRF analysis). Based on the relevance for the study questions, concentration values for twelve elements were selected (ordered by concentration): Si, Al, Fe, K, Na, Ca, Mg, Ti, P, Zr, Cl, and Br. The WD-XRF results indicated that soil fractions <150 μm contained OM, and LOI analysis was therefore conducted on these size fractions, these results are included in A.Table 1 (LOI, %).

Silicon is the most commonly occurring element, with an average concentration of 30 ± 15 wt%. The Si concentration generally increases with increasing grain size up to250 μm, after which the trend levels off (A.Table 1). Potassium (2 ± 1%) and Na (2.5 ± 2%) also follow a similar pattern. The highest Si content is observed in the size fraction above 150 μm of the dune samples (9AB, 11B). The variability of Al is relatively low throughout the data-set, with average values around 6 ± 2%. Somewhat lower Al values were noted in the two dune samples (9AB and 11B, ~5%). Iron (4 ± 2%), Ca (1.5 ± 1.5%), Ti (1 ± 2‰), Zr (0.5 ± 1‰), and Mg (0.5 ± 1%) display similar variability in concentrations, first increasing sharply from the finest grain size (<38 μm), peaking either in the size fraction 63–150 μm (1A, 3A, 7A, 8B, 9AB) or 150–250 μm (6B), followed by decreasing concentration values with increasing grain size. Phosphorus (1 ± 2‰), Cl (113 ± 178 ppm), and Br (26 ± 110 ppm) decrease sharply with increasing grain size and decreasing OM content.

The Si/Ti ratio displays a large range (min: 6, max: 933), which varies both with grain size as well as soil type. The dune samples display the highest values, as well as the largest ratio variability, of all the analyzed samples (A.Table 1). In all the source samples, the ratio is markedly lower below 150 μm (average: 36) compared to above this size class (average: 199). In four samples (1A, 6B, 7A, 9B) minimum ratios are observed in the 63–150 μm size fraction, reflecting a higher Ti content in these samples. The Si/Al ratio average is 5 ± 3.3, and generally increases with increasing size fractions (6 out of 7 samples) until 250 μm after which the increase levels off. Again, distinct values are reported for both dune samples, with overall higher Si/Al ratios reported above 63 μm. In sample 9AB a steeper Si/Al increase is observed with increasing grain size, while 11B (which lacks data for the <63 μm fraction) shows a decreasing Si/Al ratio trend with increasing grain size.

The results of the PCA of the surface source data show that three components explain 82% of the variability (Table 3). The first component (CP1) captures 36% of the variance and strongly associated (>0.7)

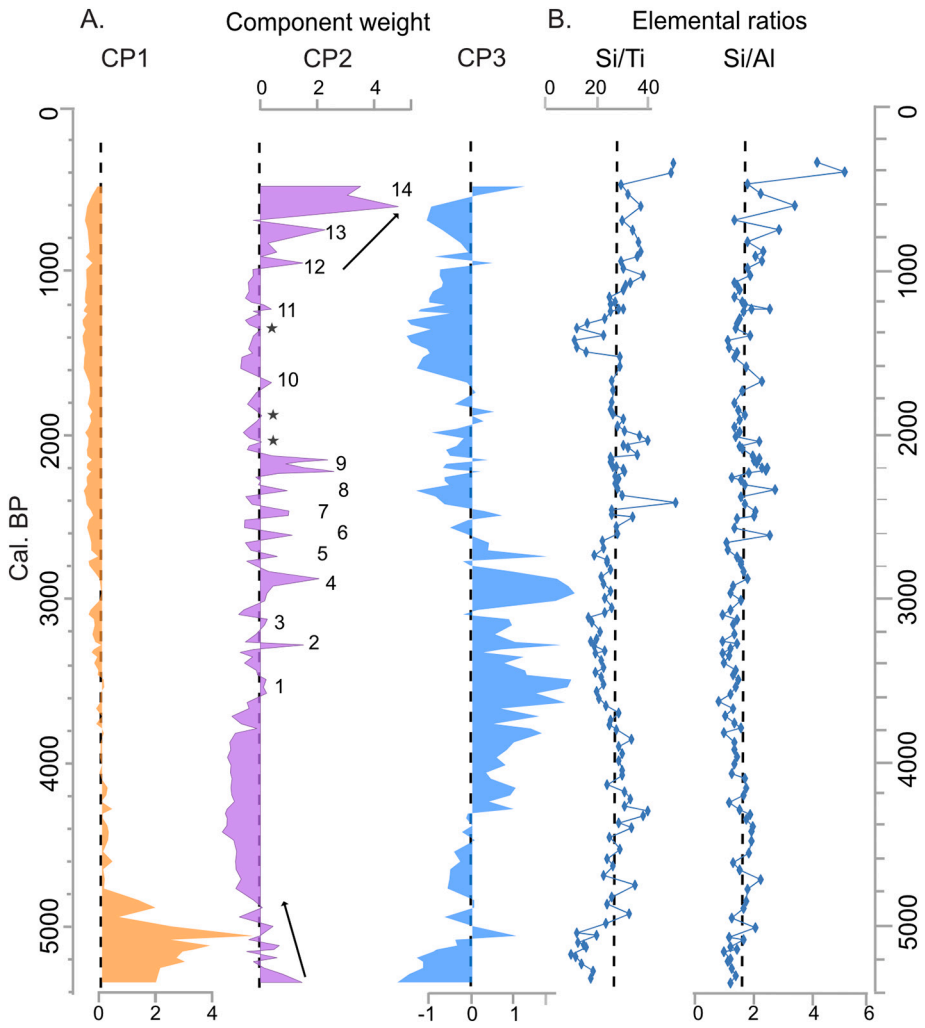

Fig. 4. (A.) Weight components (CP), throughout the sequence. (B.) Elemental mass ratios Si/Ti and Si/Al. Dust events (CP2 > 0.1) are numbered 1–14, smaller events (>0.01) indicated by stars. (For interpretation of the references to color in this figure legend, the reader is referred to the web version of this article.)

Table 3
Result of PCA analysis of elemental concentrations in local source samples.

Variable	CP1	CP2	CP3
Expl. var. %	36	32	15
Cum. var. %	36	68	82
Ti	**0.94**	0.13	−0.08
Fe	**0.92**	0.23	0.10
Ca	**0.91**	−0.04	0.16
Zr	**0.85**	0.05	−0.27
Mg	**0.83**	0.15	0.18
P	0.15	**0.89**	−0.17
Cl	0.11	**0.87**	0.11
Br	−0.19	**0.85**	−0.21
Al	0.24	−0.09	**0.85**
K	−0.35	−0.62	0.63
Na	−0.10	−0.64	0.60
Si	−0.31	**−0.82**	0.16

elements include Ti, Fe, Ca and Zr. The second component (CP2) captures 32% of the variance and strongly (positively) associated variables include P, Cl and Br, while Si is strongly negatively associated. Sodium and K display a moderate negative association to CP2. The third component captures 15% with a strong association of Al and moderate associations of K and Na.

3.4. pXRD mineral analysis and SEM-EDS

3.4.1. Peat sequence

The results of the peat pXRD analysis ($n = 16$) and Rietveld refinement quantification are summarized in Table 4. Albite and oligoclase are here presented under their group name, plagioclase, since they are difficult to separate by pXRD analysis alone due chemical similarity and substitution (solid solution, e.g., Moore and Reynolds, 1997). The group term alkali feldspars includes microcline and orthoclase and the mineral group mica here includes biotite, muscovite and vermiculite. The term "iron oxide" is here used for magnetite, because this phase may have formed during the pre-treatment (ashing, 500 °C) (Brindley and Brown, 1984). The remaining phases are presented by their assigned mineral names (Whitney and Evans, 2010). Throughout the sequence a layered double hydroxide-like (LDH) mineral was identified (Constantino and Pinnavaia, 1995; Frost et al., 2009; Iorio et al., 2010; Mills et al., 2012), which is an uncommon mineral in granitic settings, but may have formed as a secondary mineral after Ca-plagioclase weathering (Hangx and Spiers, 2009), or during the pre-treatment (ashing, 500 °C). This phase has previously been identified in peat sequences, co-occurring with calcite, both likely having an authigenic origin (Sjöström et al., 2020).

In the peat sequence, the lowermost part (5290–4100 cal BP) is dominated by iron oxides and LDH, together with the occurrence of quartz (<20%). A similar composition is observed at 3460 cal BP,

Table 4
Result of XRD mineral identification and Rietveld refinement quantification. A ratio between total quartz and feldspar content is also displayed (Qz/Fs).

Cal BP *AD*	Sample	Qz	Pl	Afs	Qz/Fs	Amp	Mica	Clay	LDH	Iron oxides	Un.	R_{wp}
2020	2020A	35	33	27	0.6	4	1	*				14.7370
420	C1, 5–7	48	27	22	1.0		3				*	11.1226
910	C1, 41–42	64	19	12	2.1		5			*		9.7463
960	C1, 45–46	36	10	14	1.5		*		39			9.7381
1240	C1, 66–67	61	13	22	1.7		1		3			10.6331
1590	C2, 23–24	18	8	5	1.4		1		68			12.1359
1720	C2, 34–35	32	8	4	2.8		1		55			11.8375
2160	C2, 70–71	48	12	22	1.4		*		18			11.7182
2500	C3, 34–35	34	6	1	4.9		*		57			14.9269
2890	C3, 76–77	33	6	3	3.7		1		57	*		14.0498
3100	C4, 23–24	70							22		*	9.3790
3460	C4, 63–64	21	11						68			10.9432
4100	C5, 61–62	8							53	39		8.3685
4200	C5, 71–72	18							39	42		8.8474
4860	C6, 58–59	8							2	83	*	7.6016
5290	C7, 95–96	10								87		7.5713

Qz; quartz. Pl: plagioclase. Afs: Akali feldspar. Amp: Amphibole. Mica: bitotite, muscovite and/or vermiculite. LDH: layered double hydroxides (hydrotalcite). Iron oxides: Magnetite. Unkn: unkown. * = occurrence. Abbreviations follow (Whitney and Evans, 2010). R_{wp} is a discrepancy value between the data and the model (Toby, 2006).

together with the presence of plagioclase. At 3100 cal BP only two phases dominate: quartz and LDH. In the samples from 3000 cal BP towards the present, more felsic minerals are noted (quartz, plagioclase, alkali feldspar, mica), with the LDH remaining a major constituent until *c.* 1200–1000 cal BP. The relative quartz to feldspar ratio was calculated for all the samples (Table 4, Qz/Fs) showing values ranging from 0.6 (surface) to 4.9 (2500 cal BP). The sample from the current bog surface (2020A) included quartz, plagioclase and alkali feldspars, amphibole, mica and a minor occurrence of clay minerals. To verify the pXRD mineral phase identification, one sample, C3 34–35, was also analyzed by SEM-EDS. The analysis confirmed, based on the chemical composition (A.Fig. 3), that quartz, plagioclase, alkali feldspars and a fine-grained LDH-like phase (Mg, Al) dominated the sample composition. In addition to these dominant phases, occurrence of chlorite, rutile, biotite and monazite was observed (A.Fig. 3).

3.4.2. Source samples

The results of the local source pXRD analysis and Rietveld refinement quantification are summarized in Table 5 ($n = 24$). Quartz, plagioclase and alkali feldspar were identified in all subsamples. Plagioclase is the most commonly occurring phase, followed by quartz and alkali feldspars, amphiboles, mica and chlorite. Plagioclase content increases with increasing grain size until 500 μm in the till (3A and 8B) and glaciofluvial sample, while the dune sample (9AB) shows the reverse trend. Alkali feldspars decrease with increasing grain size, in contrast to the elemental data where increased K content was observed with increasing grain size (A.Table 1), likely related to a relative enrichment of plagioclase feldspars. In the till (3A, 8B) and dune sample (9AB) quartz content increases with increasing grain size. The glaciofluvial sample (6B) displays a higher quartz content in the finer-grain sizes (38–63 μm and < 38 μm) compared to above 63 μm. Amphiboles were identified in the majority of samples (39 of 40) and occur in relatively higher

Table 5
Result of pXRD mineral analysis and Rietveld refinement quantification for selected source samples. Soil type code: (1) = glaciofluvial sediments, (2) = till, (3) = aeolian dune).

Id	Size, μm	Qz	Pl	Afs	Qz/Fs	Amp	Mica	Chl.	Clay	Ilm	Sd	R_{wp}
3A	<38	25	42	23	0.4	10		1	1			10.2365
(2)	38–63	31	41	24	0.5	3		1				12.8403
	63–150	31	45	21	0.5	3				*		16.5156
	150–250	36	43	19	0.6	1		*	*			19.9261
	250–500	36	45	17	0.6	2		*				17.6279
	>500	31	44	22	0.5	2	*	*				18.6596
6B	<38	42	31	24	0.8	3	1					8.6897
(1)	38–63	38	34	23	0.7	3	2					9.2404
	63–150	30	40	23	0.5	4	4					11.7432
	150–250	30	47	20	0.4	3	*					16.9602
	250–500	30	47	20	0.4	3	*	*				16.9602
	>500	25	44	29	0.3	*	*	*				21.3915
8B	<38	26	32	26	0.4	14		3				9.8602
(2)	38–63	29	39	23	0.5	8		1				11.2908
	63–150	26	41	24	0.4	8		*				14.3522
	150–250	32	41	20	0.5	6		1				16.7413
	250–500	29	44	19	0.5	7	*	*	*			16.2583
	>500	20	53	13	0.3	11	*	*	*			16.8155
9AB	<38	17	54	22	0.2	7		1				10.1308
(3)	38–63	15	52	21	0.2	11		*				15.2594
	63–150	24	44	13	0.4	18				*	*	17.7278
	150–250	46	41	12	0.9	*						21.6098
	250–500	52	33	15	1.1	*						16.7964
	>500	52	33	15	1.1	*						20.8313

Qz; quartz. Pl: plagioclase feldspar. Afs: Akali feldspar. Amp: Amphibole. Mica: bitotite, muscovite and/or vermiculite. Chl: chlorite. Clay: kaolinite or smectite. Ilm: ilmenite. * ≤1% occurrence. Mineral abbreviations follow (Whitney and Evans, 2010). R_{wp}: discrepancy index between the fitted model and data (Toby, 2006).

concentrations in grain sizes below 150 μm (3A, 6B, 9AB). Mica minerals, chlorite and ilmenite were identified in minor amounts throughout all samples, without any clear relationship with grain size or soil type. The mineral composition observed in these surface samples are in line with a previous study where soil chemistry and mineral composition at twelve locations around the Halland province were studied (Sjöström and Lin, 1996). The SEM-EDS analysis of sample 3A > 500 μm, confirmed, based on the chemical composition (A.Fig. 4) that quartz, albite, microcline and amphibole dominated the sample. In addition to the dominant phases identified by pXRD, minor occurrences of ilmenite, apatite, magnetite, diopside, rutile and titanite were also observed (A. Fig. 4).

4. Discussion

4.1. Deposit characterization

The oldest part of the sequence (~5350–5230 cal BP) consists of woody *Carex* peat, indicating that initiation of the mire occurred through soil paludification, a common peatland initiation process in the region (Nilsson, 1968; Påsse, 1993) (Fig. 3). This was followed by a period of non-woody *Carex* peat that, together with relatively high ash, AAR, C, Ca, Fe and N contents, indicates that fen conditions prevailed until ~4760 cal BP (Charman et al., 2015; Shotyk, 1988). From ~4760 cal BP the ash, AAR, C, N, Ca and Fe contents drop and *Sphagnum* mosses appear (Fig. 3), indicating a shift towards ombrotrophic conditions. *Sphagnum* mosses thereafter dominate the sequence, with sedges co-occuring at times.

This peat record displays a relatively linear age model (Fig. 2), also reflected in a strong co-variability of bulk density and peat accumulation rate (Fig. 3). The peat accumulation rate is generally higher in the fen (121 ± 42 g m^{-2} yr^{-1}, $n = 50$), compared to the bog phase (73 ± 42 g m^{-2} yr^{-1}, $n = 431$). Peat decomposition and accumulation rates are affected by several factors, including vegetation, temperature, successional stage, moisture access, nutrient availability and fire occurrence (Yu et al., 2010; Charman et al., 2013; Hansson et al., 2013; Loisel et al., 2014; Schillereff et al., 2021), with a stronger relationship with nutrient (P), temperature and moisture availability on millennial timescales (Charman et al., 2015; Schillereff et al., 2021). The relatively stable peat accumulation rate at Davidsmosse (Fig. 2) suggests that during the studied period conditions stayed within the temperature and precipitation envelope required for stable peat accumulation at the site. This is also reflected in a generally high C/N ratio, a commonly used decomposition proxy (Kuhry and Vitt, 1996). In addition to the general trends outlined in section 3.2, drops in the C/N ratio co-occur with mineral dust events, discussed further below. Highly elevated ash and lithogenic element input are noted in the most recent part of the sequence (Fig. 3, Fig. 5).

4.2. Geochemical and mineralogical character of the peat sequence

The PCA of the elemental, AAR and bulk density data shows that three CP capture 85% of the total variance (Table 2). The first component (CP1) displays elevated scores in the oldest part of the sequence

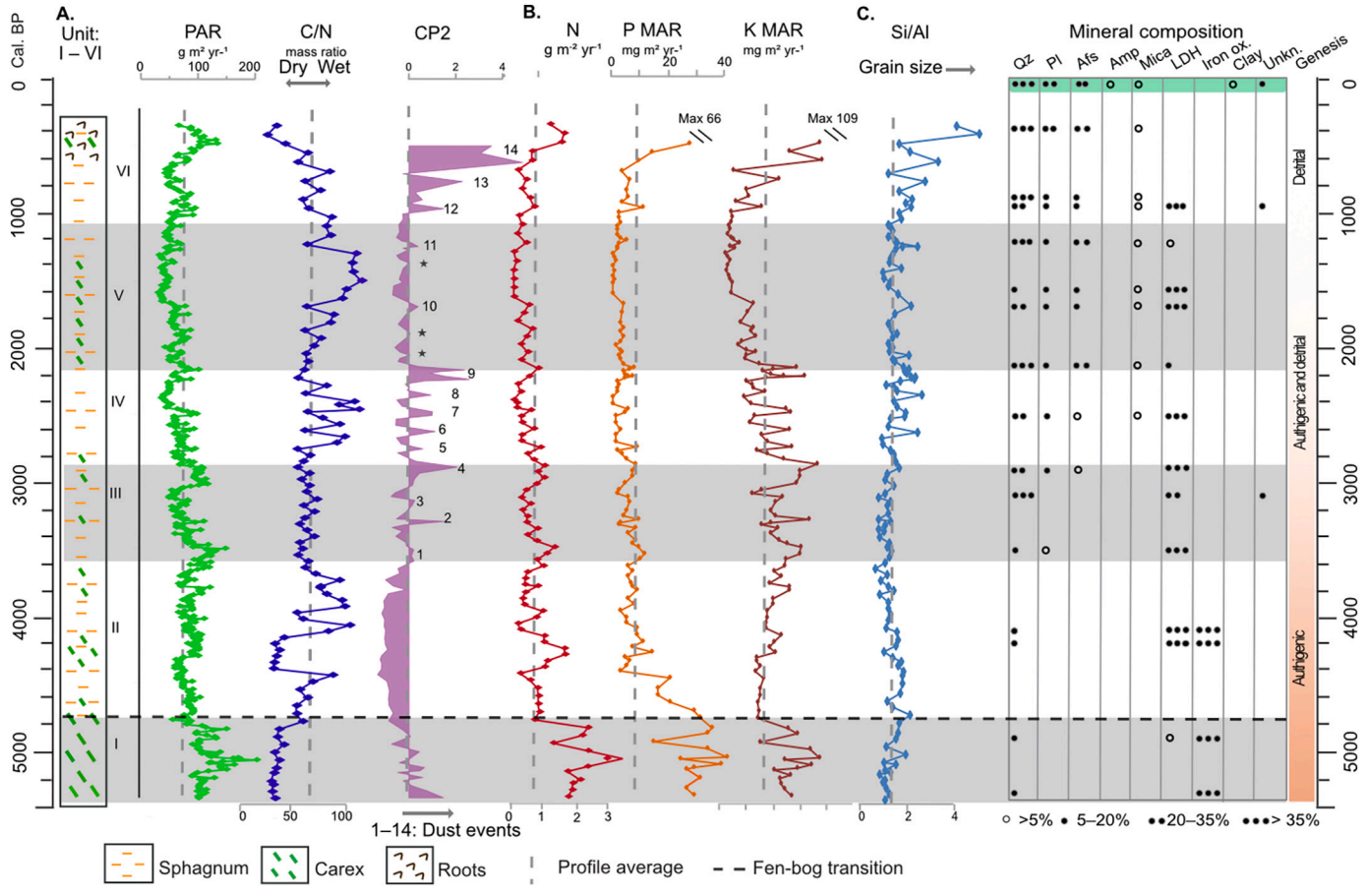

Fig. 5. Summary figure. (A.) Peat stratigraphy, peat accumulation rate (PAR), ash accumulation rate (AAR), C/N ratio and mineral dust events at Davidsmosse. (B.) Downcore nutrient content (N, P and K MAR). (C.) Inferred grain size changes (Si/Al) and relative mineral occurrence (based on Table 4, values rounded to nearest 5), and information on the genesis of the dominant mineral assemblage.(For interpretation of the references to color in this figure legend, the reader is referred to the web version of this article.)

with a strong decreasing trend upwards through the profile (Fig. 4) with Fe, Ca, AAR, S, bulk density and P as strongly associated variables. Iron, Ca, P and S occur in higher concentrations in the fen peat, which can be explained by the presence of geogenic groundwater and contact with the underlying sediments (Shotyk, 1988; Malmer, 1988; Steinmann and Shotyk, 1997). The AAR is also generally higher in the fen compared to the bog (Fig. 3), which reflects a greater relative contribution of Fe and Ca in the ash residues. The high Fe content and dominance of iron oxides (Table 4) in the mineral assemblage indicate that oxic conditions prevailed, at least seasonally, as iron oxides precipitate in the presence of oxygen (Shotyk, 1988), indicating that authigenic minerals dominate in the oldest part of the sequence (Fig. 5). That the bulk density is also associated with CP1 reflects the higher density of the more-easily degradable Carex peat (Biester et al., 2014).

The second component (CP2) includes the lithogenic elements Si, Al and Ti. In peat paleodust studies, conservative lithophile elements (e.g., Al and Ti) are commonly used as proxies for atmospheric mineral dust input (Steinmann and Shotyk, 1997; Shotyk et al., 2002; Aubert et al., 2006). Silicon can be of biogenic origin (e.g., phytoliths, diatoms) but the strong association with Al and Ti in Davidsmosse indicates that most of the Si variance is related to detrital mineral phases, which is supported by the absence of amorphous Si peaks in the downcore pXRD data, and absence of biogenic Si particles in the SEM-EDS results. We therefore interpret the above-average scores of CP2 as reflecting periods of detrital mineral deposition, with fourteen periods/peaks of elevated mineral input (DE1–14) observed in the ombrotrophic part of the sequence (Fig. 4). The DEs are also coupled to increasing Si/Al ratios, and higher Qz/Fs ratios (Table 4, Fig. 5), particularly after 3000 cal BP.

Between 4760 and 3000 cal BP, when mineral deposition was generally low, authigenic iron oxides and LDH dominate the mineral assemblage (Fig. 5). Between 3000 and 420 cal BP typically felsic minerals are identified: quartz, plagioclase, alkali feldspar and micas, together with varying occurrence of LDH (Table 4, Fig. 5). In the surface bog sample (Table 4, 2020A) detrital minerals quartz, plagioclase, alkali feldspar, amphibole, mica and clay minerals were identified. When comparing the surface minerals to those in the peat sequence we note that neither amphiboles nor clay minerals were detected, indicating these minerals weathered rapidly in the peat.

The third component (CP3) captures the main variance of Mg, Na and Cl, all of which can be associated with sea salt spray (Malmer et al., 1992), a phase that is typically not stable in the peat. The distribution of these elements in the peat is believed to be governed by changes in cation exchange capacity, which differs with both dominant vegetation and decomposition (Malmer, 1988). However, CP3 does not co-vary with either the decomposition proxies (bulk density, C/N ratios) or vegetation changes, indicating that some other process, at least partly, controls the variations in this component.

A few elements are associated with more than one CP (Br, Cl, K, Na and Sr), suggesting a complex fate in the peat. This may also reflect that they are bound to multiple phases, e.g., salt spray, soluble and insoluble minerals, organically bound etc., that are subject to different post-depositional processes.

4.3. Geochemical and mineralogical character of the potential source samples

Iron, Ca, Ti, Zr and Mg in the source samples are associated with the same component in the PCA analysis (CP1, Table 3) and generally occur in greater concentrations in the <150 μm sizes compared to the coarser grain sizes, with highly elevated concentrations of Ti noted in the 63–150 μm size fraction in four samples (1A, 6B, 7A, 9AB). Potential mineral hosts of these elements identified by the pXRD (Table 5), or SEM-EDS analysis (A.Fig. 3, A.Fig. 4), include: amphiboles (mainly pargasite ($NaCa_2(Mg_4Al)Si_6Al_2O_{22}(OH)_2$) and Mg-hornblende ($Ca_2(Mg_4Al)(Si_7Al)O_{22}(OH)_2$), biotite ($K(Mg,Fe)_3AlSi_3O_{10}(OH)_2$), ilmenite ($FeTiO_3$), rutile ($TiO_2$), and zircon ($ZrO_2$). Amphiboles and biotite host Ti as an accessory element (e.g. Nesse, 2017). Taken together, the elements associated with CP1 seem to reflect a specific composition, e.g., amphiboles and heavy minerals, which are enriched below 150 μm throughout all sample types (Table 3, Table 5). Based these mineralogical association, lower Si/Ti ratios in the source samples reflect a increased occurrence of amphiboles and heavy minerals. We note that above 250 μm highly elevated Si/Ti values (>100) occur in all samples, indicating that the coarser grain sizes are depleted in Ti-bearing minerals, in line with both the findings of the pXRD quantifications (Table 5) and previous studies (Taboada et al., 2006). This trend is particularly pronounced in the dune samples (9AB and 11B), which display values above 300.

CP2 depicts the relationship between P, Cl and Br (strong positive association) and Si, Na and K (negative association), where the first group occurs in higher concentrations in the finer grain sizes while the latter group generally increases with increasing grain size (A.Table 1). Apatite was identified in the SEM-EDS analysis (A.Fig. 2.), indicating that some of the P in the source material is hosted in this mineral ($Ca_5(PO_4)_3(F,OH,Cl)$), but the strong association of P with Cl and Br also indicates an association with the higher OM content of the finer grain sizes, as Cl and Br accumulate as organo-halogens in OM (Martínez Cortizas et al., 2016). Silicon, Na and K are (negatively) associated because these elements increase in concentration with increasing grain size.

The third component (CP3) captures the major feldspar elements (strong association of Al, K and Na) (Table 3). These elements show a somewhat different pattern between the different deposits, likely reflecting different degrees of sorting and maturity in the source samples (Table 5, Nesbitt et al., 1997). The split of the major quartz and feldspar elements (Si, Al, K and Na) into two components in the PCA analysis is thus related to the somewhat different feldspar and quartz contents of the different types of deposits. The aeolian dune deposits (9AB, 11A) display the highest degree of sorting and also a higher enrichment of quartz relative to the feldspars (A.Table 1, Table 5). Si/Al ratios increase with increasing grain size in six out of seven samples (A.Table 1), showing that this ratio reflects grain size changes in the majority of source samples, in line with previous studies (Pye, 1987).

4.4. Linking the peat sequence to the potential source samples

The elemental groupings in the PCA of the source samples differ from those of the peat samples, where Si, Al and Ti are associated with the same CP in the peat (Table 2), but two different CPs in the source samples (Table 3). This likely reflects i) that the source samples were split into different size fractions whereas the peat samples represent all deposited size fractions, ii) the different settings of the two sample matrices (i.e., water-saturated, acidic, high organic content peat vs mainly inorganic soils) and iii) distinct transport processes. Some elements are also linked to different processes in the two data-sets. For example, Ca is associated with upwards diffusion in the peat, while Ca in the soil samples is related to a specific mineral composition. In addition, many minerals are weathered in the acidic peat, such as carbonates, apatite (Le Roux et al., 2006), amphiboles and clay minerals (this study, see section 4.2). These factors and resulting differences in elemental associations in the different sample matrices need to be considered when comparing the two data-sets.

The pXRD results show that the local surface samples around Davidsmosse are dominated by quartz, plagioclase, alkali feldspars, mica and amphiboles together with minor occurrences of ilmenite, rutile, zircon and apatite (Table 5, A.Fig. 4). A similar mineral composition was also identified at the bog surface (Table 4). The Rietveld quantification shows that the detrital mineral sample from the bog surface (Table 4, sample 2020A) consists of quartz (35%), plagioclase (33%), alkali feldspar (27%), amphibole (4%), mica (1%) and the presence of clay minerals (broad peaks at ~12 and ~ 7 Å). The relative distribution between quartz, feldspars, amphiboles and micas deposited

on the bog are more similar to the till and glaciofluvial sediments close to the bog (samples 3A and 6B, within 1.5 km radius) compared to the till located 4 km west of the bog (8A) or the aeolian dune (9AB). Furthermore, we note that source sample 6B (glaciofluvial sediment, directly north of the bog) is the sample that displays the most similar composition, with the grain size between 38 and 63 μm being most similar (38% quartz, 34% plagioclase, 23% alkali feldspar, 3% amphibole and 2% mica; Table 5). Due to weathering, direct source identification based on the mineral assemblage in the peat is prevented, and instead the ratios of lithogenic elements (Si/Ti, Si/Al), with support of the pXRD data (Table 4), will be explored.

When comparing the Si/Ti ratio of the peat profile with the source samples we find that the average in the non-dust events is ~26, and that the DEs are somewhat elevated (~28), with the uppermost parts of the sequence displaying significantly higher values (~50). Most source samples and grain sizes display either higher or lower values, but two source samples, namely 6B (63–150 μm and 150–250 μm) and 9AB (<38 μm and 38–63 μm) display somewhat similar ratios (24). For the uppermost part of the sequence, where higher Si/Ti values are noted, it is again sample 6B that shows the most similar ratio value (49, 250–500 μm), indicating that coarse particles and a local source, located within 1.5 km from the bog, provided the bulk of the minerals deposited around 400 cal BP. A period of decreased Si/Ti ratios (~13) is noted around 1400 cal BP, indicating increased input of Ti-bearing minerals during this period.

The Si/Al ratios in the peat sequence average around 1.8, whereas the average value in the soil samples is 5 (Fig. 4, A.Table 1). This difference might be a result of mineral weathering in the peat (i.e., amphibole, Ca-plagioclase) and the presence of authigenic minerals (LDH) dominated by Mg and Al (A.Fig. 3). Nevertheless, elevated Si/Al values in both the peat and the surface soil samples coincide with increased occurrences of quartz and plagioclase, which from the analysis of the surface samples, as well as previous studies (Pye, 1987) is associated with increasingly coarse particles. It should be noted that relative enrichment of quartz over feldspars could also indicate feldspar weathering (Nesbitt et al., 1997), but the presence of more weathering susceptible minerals (e.g., chlorite, biotite, A.Fig. 4), in combination with the sharp increases compared to background values during DEs, rather points towards a grain-size shift during DEs. In support of this interpretation, previous studies from the Halland province, ~30 and ~60 km south of our study site, also found coarse particles (>200 μm) deposited in bogs during the same periods as many of the DEs identified here (Björck and Clemmensen, 2004; de Jong et al., 2006). Based on the Si/Al ratio, the coarsest minerals were deposited during the last DE (DE14, *c.* 620–360 cal BP).

4.5. Nutrient content in the peat sequence and source samples

Bogs are nutrient-limited ecosystems, deficient in N, P and K (Malmer, 1988; Malmer and Wallén, 2004; Limpens et al., 2006; Wieder and Vitt, 2006), with other macronutrients (e.g., Ca and Mg) also potentially being important (Bauer et al., 2011; Wang et al., 2015). In this study, the majority of DE are coupled to elevated peat accumulation rates. By exploring the concentration of these elements in the peat sequence and local sources we can consider the potential role of dust fluxes as nutrient providers. While N MAR in peat sequences largely reflect past deposition rates, P and K are typically recycled in the acrotelm by the living plants (Malmer and Wallén, 2004; Limpens et al., 2006; Wieder, 2006; Schillereff et al., 2021)(Fig. 5), but elevated P deposition is still reflected by increased burial in the catotelm (Schillereff et al., 2021), and K behaves as an conservative lithogenic element below the acrotelm (Kylander et al., 2013; Sjöström et al., 2020). With this in mind, downcore variability can be indicative of relative (but not absolute) P and K deposition. At Davidsmosse, the DEs are associated with increases in N, P and K MAR (A.Fig. 2, Fig. 5, B). In the source samples P is enriched in the finer grain sizes, likely associated with both organic matter and apatite (Table 3, A.Table 1, A.Fig. 3), while K content increases with grain size, likely related to alkali feldspar and mica minerals (A.Table 1). Mica minerals were identified (biotite, muscovite) in both the peat and source samples, but less mica was observed in the peat samples, indicating weathering losses in the peat. Despite the fact that the N content was not analyzed in the soil samples, the variability of the peat N MAR profile indicates that the DEs also contained this element (Fig. 5). In general, the grain sizes <150 μm contained higher OM concentrations and amphiboles, which rapidly weather and release Ca and Mg to the peat (together with Al, Fe, Si; Table 5, A.Table 1). Taken together, the increases of N, P and K contemporary with the DEs (Fig. 5), and that the local sources contain these nutrients, both in minerals that rapidly weather in peat (apatite, amphiboles, mica, Ca-plagioclase) and in organic form, indicate that the aeolian dust fluxes contributed with elements of nutrient value to the bog ecosystem.

4.6. Dust events and bog development

Based on the occurrence of the DE, together with peat accumulation rate, AAR and C/N ratios, we divided the peat sequence into units I to VI (Fig. 5). The first unit (I: 5540–4760 cal BP) represents the fen stage with a mineral assemblage that is dominated by authigenic iron oxides. Early in the ombrotrophic stage (Unit II: 4760–3630 cal BP), low levels of detrital mineral deposition are recorded, and authigenic minerals continue to dominate (LDH, iron oxides, see section 3.4 and 4.2). The C/N profile shows an increasing trend that is interrupted by lower values between 4370 and 4140 cal BP, which co-occurs with a shift to more sedges. This period coincides with the 4.2 Ka event, which marks the transition to the late Holocene, when an onset of colder and wetter conditions has been recorded in northern Scandinavia (Walker et al., 2019). During this period, low levels of mineral deposition were also inferred at bogs located both in the Halland region, as well as further inland (Björck and Clemmensen, 2004; Kylander et al., 2016; Sjöström et al., 2020).

In Unit III (3580–2800 cal BP) there are three short episodes (DE1–3 centered on 3500, 3280; and 3140 cal BP) and one DE of longer duration (DE4, 3010–2835 cal BP) (Fig. 5). Increases in peat accumulation rates are recorded during all four events, while the C/N ratio stays close to the average, indicating little change in decomposition and/or vegetation during this unit. The Si/Al ratio is close to the average during DE1–3 indicating that the size of deposited particles did not differ much from background levels, while somewhat elevated Si/Al values, and thus grain size, are recorded during DE4.

In Unit IV (2835–2130 cal BP) five DEs occur (5–9) (Fig. 5). The earlier events are episodic in character, recorded in only one (DE5, 6, and 8) or two (DE7) samples, while DE9 is more prolonged (n=8, 2240–2130 cal BP). All the DEs in Unit IV co-occur with increasing Si/Al ratios, indicating that relatively coarser minerals were deposited during these events. The DEs are also coupled to increases in peat accumulation rate, with the exception of DE8. The C/N ratios drop in conjunction with the DEs, suggesting either that the DEs occurred during periods of episodic lowering of the water table or that the DEs affected the C/N ratio. That the peat accumulation rate increases during the DEs conflicts with the idea that the C/N ratio shift was caused by increased decomposition due to drier conditions. A closer look at the C and N MAR profiles (Fig. 3) show that both elements increase during the DEs, but that the N increase is relatively higher than C, thus driving the observed ratio decrease. The overall climate trend during this period is towards cooler and drier conditions (Borgmark, 2005; Wanner et al., 2011; Kylander et al., 2013; Sjöström et al., 2020; Martínez Cortizas et al., 2021), but the high C/N ratios and peat accumulation rates suggest that the moisture balance in the bog was maintained. Starting from *c.* 3000 cal BP regional pollen records suggest a progressive opening of the landscape (de Jong et al., 2006; Jong et al., 2009), which would lead to more exposed soils and thus an increased availability of soil particles for aeolian transport. The nearby peat records from Hyltemossen as well as

Undarsmossen (de Jong et al., 2006; Björck and Clemmensen, 2004), as well as dune formation in Denmark (Clemmensen et al., 2001), also recorded increased aeolian activity during this period.

Unit V (2070–1000 cal BP) is characterized by generally low levels of mineral deposition, with two dust events noted at 1690 (10); and 1240 cal BP (11) together with three minor increases around 2050, 1890 and 1360 cal BP. Increases in peat accumulation rates are co-occuring with the events. C/N is generally high, implying that mostly wet conditions prevailed during this period, with decreases noted during the DEs, likely related to elevated N associated with the mineral dust (Fig. 3, Fig. 5). From the Si/Al ratio, elevated grain sizes are inferred during all DEs.

Unit VI (1000–360 cal BP) is characterized by a general increase in mineral fluxes and the highest mineral input throughout the entire sequence (Fig. 5). A stepwise increase in mineral input is recorded, with peaks centered around 960 (12), 890–760 (13) and 615–490 cal BP (14). Based on the AAR profile, this latest event (DE14) continued until 360 cal BP (Fig. 3). The C/N value displays a generally decreasing trend throughout this unit, with reductions noted during the DEs. Again, increases in the Si/Al ratio are observed during the DE, indicating that increasingly coarse minerals were deposited. During this period, human activities such as forestry and agriculture intensified (de Jong and Lagerås, 2011), contributing to a more open landscape and more exposed soils. This, in combination with colder conditions during the Little Ice Age (*c.* LIA, 700 to 150 cal BP)(Wanner et al., 2011), increased sea-ice in the North Atlantic, a negative NAO, and a southward shift in winter storm tracks (Björck and Clemmensen, 2004; Olsen et al., 2012) likely contributed to the larger scale mineral input observed during DE14. Synchronous with this latest, and largest mineral peak at Davidsmosse, elevated inputs of coarser particles were also recorded in a nearby bog (Hyltemossen, Björck and Clemmensen, 2004). The latest episode contains the coarsest grains and is associated with elevated decomposition, and a shift towards more sedges indicating either that the elevated mineral input affected the plant and microbial communities, which affected the decomposition rates (Bragazza et al., 2006; Schillereff et al., 2021; Ryberg et al., 2022), or that this was a drier period, assoicated with lowered water tables.

5. Conclusions

This study presents a paleodust and peat accumulation rate record from 5400 to 360 cal BP from Davidsmosse bog, south-western Sweden, coupled with analysis of local soil dust sources. In total 14 DEs were observed, with two periods seeing particularly many, episodic, DEs dominated by coarser particles (2800–2130 and 960–360 cal BP). Previous studies have suggested increased winter storms in the region for these time periods (Björck and Clemmensen, 2004), indicating that Davidsmosse received, in addition to fine-grained mineral dust, also coarser-grained minerals deposited by winter storm events. Generally stable conditions for peat accumulation prevailed following the transition to an ombrotrophic bog, indicating that precipitation (present-day average: 1100 mm yr^{-1}) has remained high throughout the studied period. Increases in peat accumulation rates were recorded during a majority of the DEs at Davidsmosse (13 of 14). Contemporary with these events, important nutrients (N, P and K) increased, which, together with the finding that local sources contained both K and P, show that atmospheric mineral dust affect bog ecosystems, as previously suggested by (Kylander et al., 2018; Sjöström et al., 2020; Schillereff et al., 2021). However, the observed trend that DEs are coupled to elevated peat accumulation rates breaks down in the most recent part of the sequence, where highly elevated mineral input co-occurs with decreasing accumulation rates and C content, indicating that a threshold effect may have been reached (Moore et al., 2019; Schillereff et al., 2021; Ryberg et al., 2022). Future studies should include studies on grain size analysis, peat mineral weathering, and a regional aeolian activity review, which could increase the knowledge on past storminess patterns in Scandinavia, including its driving mechanisms.

Data availability

Data-sets related to this article can be found at the Bolin Centre for Climate Research repository (https://bolin.su.se/data/sjostrom-2022-davidsmosse-1).

Declaration of Competing Interest

The authors declare that they have no known competing financial interests or personal relationships that could have appeared to influence the work reported in this paper.

Acknowledgements

Three anonymous reviewers contributed with valuable feedback which improved the manuscript. Soil sampling fieldwork and analysis was funded by Willhelm Smitts foundation. Dr. Elin Tollefson (Dept. of Geological Sciences, Stockholm University) is thanked for introducing the HighScore Rietveld refinement method. Dr. Fredrik Schenk (Dept. of Geological Sciences, Stockholm University) contributed with interpretation discussions and is thanked for valuable feedback and comments. Dr. Sandra Gdaniec conducted a grain size analysis trial on peat samples from Davidsmosse and BSc Anna Virolainen conducted the WD-WD-XRF, C, N and $\delta^{13}C$ analysis. Lucky Allerby assisted during fieldwork.

Appendix A. Supplementary data

Supplementary data to this article can be found online at https://doi.org/10.1016/j.chemgeo.2022.120881.

References

Albani, S., et al., 2015. Twelve thousand years of dust: the Holocene global dust cycle constrained by natural archives. Clim. Past 11, 869–903. https://doi.org/10.5194/cp-11-869-2015.

Alexandersson, H., 2006. Vindstatistik för Sverige 1961-2004: SMHI Metrologi Nr 121. http://www.smhi.se/polopoly_fs/1.1895!/meteorologi_121-06%5B1%5D.pdf.

Aubert, D., Le Roux, G., Krachler, M., Cheburkin, A., Kober, B., Shotyk, W., Stille, P., 2006. Origin and fluxes of atmospheric REE entering an ombrotrophic peat bog in Black Forest (SW Germany): evidence from snow, lichens and mosses. Geochim. Cosmochim. Acta 70, 2815–2826. https://doi.org/10.1016/j.gca.2006.02.020.

Bauer, P., Elbaum, R., Weiss, I.M., 2011. Calcium and silicon mineralization in land plants: Transport, structure and function. Plant Sci. 180, 746–756. https://doi.org/10.1016/j.plantsci.2011.01.019.

Biester, H., Knorr, K.-H., Schellekens, J., Basler, A., Hermanns, Y.-M., 2014. Comparison of different methods to determine the degree of peat decomposition in peat bogs. Biogeosciences v. 11, 2691–2707. https://doi.org/10.5194/bg-11-2691-2014.

Björck, S., Clemmensen, L.B., 2004. Aeolian sediment in raised bog deposits, Halland, SW Sweden: a new proxy record of Holocene winter storminess variation in southern Scandinavia? The Holocene 14, 677–688. https://doi.org/10.1191/0959683604hl746rp.

Blaauw, M., Christen, J.A., 2011. Flexible paleoclimate age-depth models using an autoregressive gamma process: Bayesian. Analysis 6, 457–474. https://doi.org/10.1214/11-BA618.

Borgmark, A., 2005. Holocene climate variability and periodicities in south-central Sweden, as interpreted from peat humification analysis. The Holocene 15, 387–395. https://doi.org/10.1191/0959683605hl816rp.

Bragazza, L., et al., 2006. Atmospheric nitrogen deposition promotes carbon loss from peat bogs. Proc. Natl. Acad. Sci. v. 103, 19386–19389. https://doi.org/10.1073/pnas.0606629104.

Brindley, G.W., Brown, G., 1984. Crystal structures of clay minerals and their X-ray identification: London. Mineral. Soc. 2, 1–495.

Charman, D.J., et al., 2013. Climate-related changes in peatland carbon accumulation during the last millennium. Biogeosciences 10, 929–944. https://doi.org/10.5194/bg-10-929-2013.

Charman, D.J., Amesbury, M.J., Hinchliffe, W., Hughes, P.D.M., Mallon, G., Blake, W.H., Daley, T.J., Gallego-Sala, A.V., Mauquoy, D., 2015. Drivers of Holocene peatland carbon accumulation across a climate gradient in northeastern North America. Quat. Sci. Rev. 121, 110–119. https://doi.org/10.1016/j.quascirev.2015.05.012.

Clemmensen, L.B., Murray, A.S., Bech, J.-H., Clausen, A., 2001. Large-scale aeolian sand movement on the west coast of Jutland, Denmark in late Subboreal to early Subatlantic time—a record of climate change or cultural impact? GFF 123, 193–203. https://doi.org/10.1080/11035890101234193.

Constantino, V.R.L., Pinnavaia, T.J., 1995. Basic properties of Mg2+1-xAl3+x layered double hydroxides intercalated by carbonate. Hydroxide, Chloride, and Sulfate Anions: Inorganic Chemistry 34, 883–892. https://doi.org/10.1021/ic00108a020.

de Jong, R., Lagerås, P., 2011. Exploring the patterns and causes of land use changes in south-West Sweden. Veg. Hist. Archaeobotany 20, 15–27. https://doi.org/10.1007/s00334-010-0269-8.

de Jong, R., Björck, S., Björkman, L., Clemmensen, L.B., 2006. Storminess variation during the last 6500 years as reconstructed from an ombrotrophic peat bog in Halland, Southwest Sweden. J. Quat. Sci. 21, 905–919. https://doi.org/10.1002/jqs.1011.

De Vleeschouwer, F., et al., 2012. A millennial record of environmental change in peat deposits from the Misten bog (East Belgium). Quat. Int. 268, 44–57. https://doi.org/10.1016/j.quaint.2011.12.010.

Dean, W.E., 1974. Determination of carbonate and organic matter in calcareous sediments and sedimentary rocks by loss on ignition: comparison with other methods: SEPM. J. Sediment. Res. 44 https://doi.org/10.1306/74D729D2-2B21-11D7-8648000102C1865D.

Degen, T., Sadki, M., Bron, E., König, U., Nénert, G., 2014. The HighScore suite. Powder Diffract. 29, S13–S18. https://doi.org/10.1017/S0885715614000840.

Eriksson, L., Johansson, E., Katteneh-Wodl, N., Wold, S., 1999. Introduction to Multi- and Megavariate Data Analysis Using Projection Methods (PCA & PLS): Umeå. Umetrics AB.

Frost, R.L., Spratt, H.J., Palmer, S.J., 2009. Infrared and near-infrared spectroscopic study of synthetic hydrotalcites with variable divalent/trivalent cationic ratios. Spectrochim. Acta A Mol. Biomol. Spectrosc. 72, 984–988. https://doi.org/10.1016/j.saa.2008.12.018.

Givelet, N., et al., 2004. Suggested protocol for collecting, handling and preparing peat cores and peat samples for physical, chemical, mineralogical and isotopic analyses. J. Environ. Monit. 6, 481–492. https://doi.org/10.1039/B401601G.

Gu, C., Hart, S.C., Turner, B.L., Hu, Y., Meng, Y., Zhu, M., 2019. Aeolian dust deposition and the perturbation of phosphorus transformations during long-term ecosystem development in a cool, semi-arid environment. Geochim. Cosmochim. Acta v. 246, 498–514. https://doi.org/10.1016/j.gca.2018.12.017.

Hangx, S.J.T., Spiers, C.J., 2009. Reaction of plagioclase feldspars with CO2 under hydrothermal conditions. Chem. Geol. 265, 88–98. https://doi.org/10.1016/j.chemgeo.2008.12.005.

Hansson, S.V., Rydberg, J., Kylander, M., Gallagher, K., Bindler, R., 2013. Evaluating paleoproxies for peat decomposition and their relationship to peat geochemistry. The Holocene v. 23, 1666–1671. https://doi.org/10.1177/0959683613508160.

Harrison, S.P., Kohfeld, K.E., Roelandt, C., Claquin, T., 2001. The role of dust in climate changes today, at the last glacial maximum and in the future. Earth Sci. Rev. 54, 43–80. https://doi.org/10.1016/S0012-8252(01)00041-1.

Iorio, M., De Martino, A., Violante, A., Pigna, M., Capasso, R., 2010. Synthesis, characterization, and sorption capacity of layered double hydroxides and their complexes with polymerin. J. Agric. Food Chem. 58, 5523–5530. https://doi.org/10.1021/jf904092n.

Jong, R.D., Hammarlund, D., Nesje, A., 2009. Late Holocene effective precipitation variations in the maritime regions of south-west Scandinavia. Quat. Sci. Rev. 11. https://doi.org/10.1016/j.quascirev.20 08.09.014.

Knippertz, P., Stuut, J.-B.W. (Eds.), 2014. Mineral Dust: A Key Player in the Earth System. Dordrecht, Springer Netherlands. https://doi.org/10.1007/978-94-017-8978-3.

Kuhry, P., Vitt, D.H., 1996. Fossil carbon/nitrogen ratios as a measure of peat decomposition. Ecology 77, 271–275. https://doi.org/10.2307/2265676.

Kylander, M., Weiss, D., Martinezcortizas, A., Spiro, B., Garciasanchez, R., Coles, B., 2005. Refining the pre-industrial atmospheric Pb isotope evolution curve in Europe using an 8000 year old peat core from NW Spain. Earth Planet. Sci. Lett. v. 240, 467–485. https://doi.org/10.1016/j.epsl.2005.09.024.

Kylander, M.E., Bindler, R., Cortizas, A.M., Gallagher, K., Mörth, C.-M., Rauch, S., 2013. A novel geochemical approach to paleorecords of dust deposition and effective humidity: 8500 years of peat accumulation at Store Mosse (the “Great Bog”), Sweden. Quat. Sci. Rev. 69, 69–82. https://doi.org/10.1016/j.quascirev.2013.02.010.

Kylander, M.E., Martínez-Cortizas, A., Bindler, R., Greenwood, S.L., Mörth, C.-M., Rauch, S., 2016. Potentials and problems of building detailed dust records using peat archives: an example from Store Mosse (the “Great Bog”), Sweden. Geochim. Cosmochim. Acta 190, 156–174. https://doi.org/10.1016/j.gca.2016.06.028.

Kylander, M.E., et al., 2018. Mineral dust as a driver of carbon accumulation in northern latitudes. Sci. Rep. 8, 6876. https://doi.org/10.1038/s41598-018-25162-9.

Le Roux, G., Laverret, E., Shotyk, W., 2006. Fate of calcite, apatite and feldspars in an ombrotrophic peat bog, Black Forest, Germany. J. Geol. Soc. 163, 641–646. https://doi.org/10.1144/0016-764920-035.

Li, C., Sonke, J.E., Le Roux, G., Van der Putten, N., Piotrowska, N., Jeandel, C., Mattielli, N., Benoit, M., Wiggs, G.F.S., De Vleeschouwer, F., 2020. Holocene dynamics of the southern westerly winds over the Indian Ocean inferred from a peat dust deposition record. Quat. Sci. Rev. 231, 106169 https://doi.org/10.1016/j.quascirev.2020.106169.

Limpens, J., Heijmans, M., Berendse, F., 2006. The nitrogen cycle in Boreal Peatlands. In: Boreal Peatland Ecosystems, Berlin Heidelberg, Springer Verlag, Ecological Studies, v. 188, pp. 195–230.

Loisel, J., et al., 2014. A database and synthesis of northern peatland soil properties and Holocene carbon and nitrogen accumulation. The Holocene 24, 1028–1042. https://doi.org/10.1177/0959683614538073.

López-Buendía, A.M., Whateley, M.K.G., Bastida, J., Urquiola, M.M., 2007. Origins of mineral matter in peat marsh and peat bog deposits, Spain. Int. J. Coal Geol. 71, 246–262. https://doi.org/10.1016/j.coal.2006.09.001.

Lundqvist, J., Wohlfarth, B., 2001. Timing and east–west correlation of south Swedish ice marginal lines during the late Weichselian. Quat. Sci. Rev. 20, 1127–1148. https://doi.org/10.1016/S0277-3791(00)00142-6.

Malmer, N., 1988. Patterns in the growth and the accumulation of inorganic constituents in the sphagnum cover on ombrotrophic bogs in scandinavia. Oikos v. 53, 105. https://doi.org/10.2307/3565670.

Malmer, N., Wallén, B., 2004. Input rates, decay losses and accumulation rates of carbon in bogs during the last millennium: internal processes and environmental changes. The Holocene 14, 111–117. https://doi.org/10.1191/0959683604hl693rp.

Malmer, N., Horton, D.G., Vitt, D.H., 1992. Element concentrations in mosses and surface waters of western Canadian mires relative to precipitation chemistry and hydrology. Ecography 15, 114–128. https://doi.org/10.1111/j.1600-0587.1992.tb00015.x.

Martínez Cortizas, A., Mighall, T., Pontevedra Pombal, X., Nóva Muñfoz, J.C., Peiteado Varelal, E., Piñero Rebolol, R., 2005. Linking changes in atmospheric dust deposition, vegetation change and human activities in northwest Spain during the last 5300 years. The Holocene 15, 698–706. https://doi.org/10.1191/0959683605hl834rp.

Martínez Cortizas, A., Vázquez, C.F., Kaal, J., Biester, H., Casais, M.C., Rodríguez, T.T., Lado, L.R., 2016. Bromine accumulation in acidic black colluvial soils. Geochim. Cosmochim. Acta 174, 143–155. https://doi.org/10.1016/j.gca.2015.11.013.

Martínez Cortizas, A., López-Costas, O., Orme, L., Mighall, T., Kylander, M.E., Bindler, R., Gallego Sala, Á., 2019. Holocene Atmospheric Dust Deposition in NW Spain: The Holocene, 095968361987519. https://doi.org/10.1177/0959683619875193.

Martínez Cortizas, A., Sjöström, J.K., Ryberg, E.E.S., Kylander, M.E., Kaal, J., López-Costas, O., Bindler, R., 2021. 9000 years of change in peat organic matter composition in Store Mosse (Sweden) traced using FTIR-ATR: Boreas, v. Accepted.

Mauquoy, D., van Geel, B., 2007. Plant macrofossil method and studies: mire and peat macros. In: Elias, Scott (Ed.), Encyclopedia of Quaternary Science. Elsevier, pp. 2315–2336. https://doi.org/10.1016/B0-44-452747-8/00229-5.

Mauquoy, D., Hughes, P.D.M., van Geel, B., 2010. A Protocol for Plant Macrofossil Analysis of Peat Deposits, p. 5.

Mills, S.J., Christy, A.G., Génin, J.-M.R., Kameda, T., Colombo, F., 2012. Nomenclature of the hydrotalcite supergroup: natural layered double hydroxides. Mineral. Mag. 76, 1289–1336. https://doi.org/10.1180/minmag.2012.076.5.10.

Moore, M.D., Reynolds, C.R., 1997. X-ray Diffraction and the Identification and Analysis of Clay Minerals: Oxford. Oxford University Press, UK, 332 p.

Moore, T.R., Knorr, K.-H., Thompson, L., Roy, C., Bubier, J.L., 2019. The effect of long-term fertilization on peat in an ombrotrophic bog. Geoderma 343, 176–186. https://doi.org/10.1016/j.geoderma.2019.02.034.

Nesbitt, W., Fedo, Christopher M., Young, Grant M., 1997. Quartz and Feldspar stability, Steady and Non Steady State Weathering, and Petrogenesis of Siliclastic Sands and Muds. J. Geol. 105, 173–191.

Nesse, W.D., 2017. Introduction to Mineralogy: New York. Oxford University Press.

Nilsson, E., 1968. Södra Sveriges senkvartära historia. Geokronologi, issjöar och landhöjning. Almqvist & Wiksell.

Olsen, J., Anderson, N.J., Knudsen, M.F., 2012. Variability of the North Atlantic Oscillation over the past 5,200 years. Nat. Geosci. 5, 808–812. https://doi.org/10.1038/ngeo1589.

Panait, A.M., Hutchinson, S.M., Diaconu, A.-C., Tanţău, I., Feurdean, A., 2019. Disentangling dust and sand deposition using a peat record in CE Europe (northern Romania): a multiproxy approach. Palaeogeogr. Palaeoclimatol. Palaeoecol. 532, 109257 https://doi.org/10.1016/j.palaeo.2019.109257.

Påsse, T., 1993. Description to the Quaternary Map, 115. Swedish Geological Survey Serie Ae, Ullared SO.

Pratte, S., Bao, K., Sapkota, A., Zhang, W., Shen, J., Le Roux, G., De Vleeschouwer, F., 2019. kyr of atmospheric mineral dust deposition in north-eastern China: a record of palaeoclimatic and palaeoenvironmental changes in the Chinese dust source regions. The Holocene 14. https://doi.org/10.1177/0959683619892661, 095968361989266.

Pye, K., 1987. Aeolian Dust and Dust Deposits: London. Academic Press. https://doi.org/10.1016/B978-0-12-568690-7.50001-6, 334 p.

Reimer, P.J., et al., 2020. The IntCal20 Northern Hemisphere Radiocarbon Age Calibration Curve (0–55 cal kBP). Radiocarbon 62, 725–757. https://doi.org/10.1017/RDC.2020.41.

Rietveld, 1969. A profile refinement method for nuclear and magnetic structures. J. Appl. Crystallogr. 2 https://doi.org/10.1107/S0021889869006558.

Rudmin, M., Ruban, A., Savichev, O., Mazurov, A., Dauletova, A., Savinova, O., 2018. Authigenic and detrital minerals in peat environment of vasyugan swamp, Western Siberia. Minerals 8, 500. https://doi.org/10.3390/min8110500.

Ryberg, E.E., Väliranta, M., Martinez-Cortizas, A., Ehrlén, J., Sjöström, J.K., Kylander, M.E., 2022. Postglacial peatland vegetation succession in Store Mosse bog, south-central Sweden: an exploration of factors driving species change. Boreas. https://doi.org/10.1111/bor.12580 bor.12580.

Rydberg, J., 2014. Wavelength dispersive X-ray fluorescence spectroscopy as a fast, non-destructive and cost-effective analytical method for determining the geochemical composition of small loose-powder sediment samples. J. Paleolimnol. 52, 265–276. https://doi.org/10.1007/s10933-014-9792-4.

Samuelsson, L., Larson, S.-Å., 1987. Geological map Borås: Swedish Geological Survey SGU Ser. Ba nr 41. https://resource.sgu.se/dokument/publikation/ba/ba41karta/ba41-karta.pdf.

Schillereff, D.N., Chiverrell, R.C., Sjöström, J.K., Kylander, M.E., Boyle, J.F., Davies, J.A. C., Toberman, H., Tipping, E., 2021. Phosphorus supply affects the long-term functioning of mid-latitude ombrotrophic peatlands. Commun. Earth Environ. 2 https://doi.org/10.1038/s43247-021-00316-2.

Shotyk, W., 1988. Review of the inorganic geochemistry of peats and peatland waters. Earth Sci. Rev. 25, 95–176. https://doi.org/10.1016/0012-8252(88)90067-0.

Shotyk, W., Weiss, D., Kramers, J.D., Frei, R., Cheburkin, A.K., Gloor, M., Reese, S., 2001. Geochemistry of the peat bog at Etang de la Gruère, Jura Mountains, Switzerland, and its record of atmospheric Pb and lithogenic trace metals (Sc, Ti, Y, Zr, and REE)

since 12,370 14 C yr BP. Geochim. Cosmochim. Acta 65, 2337–2360. https://doi.org/10.1016/S0016-7037(01)00586-5.

Shotyk, W., Krachler, M., Martinez-Cortizas, A., Cheburkin, A.K., Emons, H., 2002. A peat bog record of natural, pre-anthropogenic enrichments of trace elements in atmospheric aerosols since 12 370 14 C yr BP, and their variation with Holocene climate change. Earth Planet. Sci. Lett. 199, 21–37. https://doi.org/10.1016/S0012-821X(02)00553-8.

Silva-Sánchez, N., Martínez Cortizas, A., López-Merino, L., 2014. Linking forest cover, soil erosion and mire hydrology to late-Holocene human activity and climate in NW Spain. The Holocene 24, 714–725. https://doi.org/10.1177/0959683614526934.

Sjöström, J., Lin, Z., 1996. Texture, chemistry, and mineralogy of acid soil profiles in Hailand, SW Sweden. GFF 118, 227–236. https://doi.org/10.1080/11035899609546258.

Sjöström, J.K., Bindler, R., Granberg, T., Kylander, M.E., 2019. Procedure for organic matter removal from peat samples for XRD mineral analysis. Wetlands 39, 473–481. https://doi.org/10.1007/s13157-018-1093-7.

Sjöström, J.K., Martínez Cortizas, A., Hansson, S.V., Silva Sánchez, N., Bindler, R., Rydberg, J., Mörth, C.-M., Ryberg, E.E.S., Kylander, M.E., 2020. Paleodust deposition and peat accumulation rates – Bog size matters. Chem. Geol., 119795 https://doi.org/10.1016/j.chemgeo.2020.119795.

SMHI, 2009. Observational Data 1991–2013: Swedish Metrological and Hydrological Institute. https://www.smhi.se/data/meteorologi/dataserier-med-normalvarden-1.7354.

SMHI, 2015, Framtidsklimat i Hallands län: SMHI Klimatologi Nr 28, 82 p., https://www.smhi.se/polopoly_fs/1.95712!/Menu/general/extGroup/attachmentColHold/mainCol1/file/Framtidsklimat_i_Hallands_län_Klimatologi_nr_28.pdf.

Steinmann, P., Shotyk, W., 1997. Geochemistry, mineralogy, and geochemical mass balance on major elements in two peat bog profiles (Jura Mountains, Switzerland). Chem. Geol. 138, 25–53. https://doi.org/10.1016/S0009-2541(96)00171-4.

Stroeven, A.P., et al., 2016. Deglaciation of Fennoscandia. Quat. Sci. Rev. 147, 91–121. https://doi.org/10.1016/j.quascirev.2015.09.016.

Taboada, T., Cortizas, A.M., Garcıa, C., Garcıa-Rodeja, E., 2006. Particle-size fractionation of titanium and zirconium during weathering and pedogenesis of granitic rocks in NW Spain, 19.

Toby, B.H., 2006. R factors in Rietveld analysis: How good is good enough? Powder Diffraction 21, 67–70. https://doi.org/10.1154/1.2179804.

Walker, M., et al., 2019. Formal subdivision of the Holocene Series/Epoch: a summary. J. Geol. Soc. India 93, 135–141. https://doi.org/10.1007/s12594-019-1141-9.

Wang, M., Moore, T.R., Talbot, J., Riley, J.L., 2015. The stoichiometry of carbon and nutrients in peat formation: C and nutrients in peat. Glob. Biogeochem. Cycles 29, 113–121. https://doi.org/10.1002/2014GB005000.

Wanner, H., Solomina, O., Grosjean, M., Ritz, S.P., Jetel, M., 2011. Structure and origin of Holocene cold events. Quat. Sci. Rev. 30, 3109–3123. https://doi.org/10.1016/j.quascirev.2011.07.010.

Whitney, D.L., Evans, B.W., 2010. Abbreviations for names of rock-forming minerals. Am. Mineral. 95, 185–187. https://doi.org/10.2138/am.2010.3371.

Wieder, Kelman R., 2006. Primary production in Boreal Peatlands. In: Boreal Peatland Ecosystems. Springer-Verlag, Berlin Heidelberg, pp. 145–159.

Wieder, R.K., Vitt, D.H. (Eds.), 2006. Boreal Peatland Ecosystems: Berlin, Springer, Ecological Studies, vol. 188, 435 p.

Wohlfarth, B., Skog, G., Possnert, G., Holmquist, B., 1998. Pitfalls in the AMS radiocarbon-dating of terrestrial macrofossils. J. Quat. Sci. 13, 9.

Yu, Z., Loisel, J., Brosseau, D.P., Beilman, D.W., Hunt, S.J., 2010. Global peatland dynamics since the Last Glacial Maximum: Global Peatlands since the LGM. Geophys. Res. Lett. 37 https://doi.org/10.1029/2010GL043584 n/a-n/a.

Yu, H., et al., 2015. The fertilizing role of African dust in the Amazon rainforest: a first multiyear assessment based on data from Cloud-Aerosol lidar and infrared pathfinder satellite observations. Geophys. Res. Lett. v. 42, 1984–1991. https://doi.org/10.1002/2015GL063040.